

# Study on the Fracture Extension Pattern of Shale Reservoir Fracturing under the Influence of Mineral Content

Weiji Sun, Mengru Hou,\* Bing Liang, Qi Liu, Hang Zhao, and Jianfeng Hao

Cite This: *ACS Omega* 2024, 9, 32525–32535

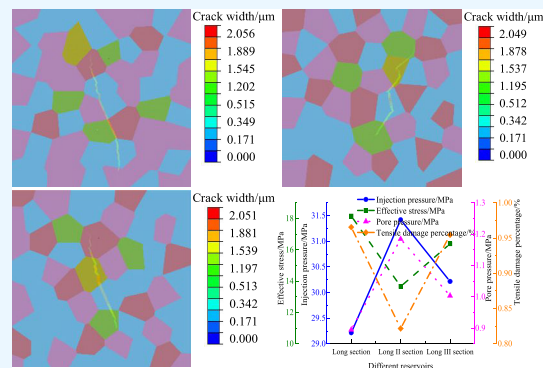
Read Online

ACCESS |

Metrics &amp; More

Article Recommendations

**ABSTRACT:** This study aimed to investigate the effect of the microstructure of shale on fracture initiation and extension during hydraulic fracturing. The Longmaxi Formation shale reservoir in the Sichuan Basin was considered as the research object; its structure was modeled from a microscopic perspective, and a zero-thickness cohesive unit was embedded within the solid unit. Numerical simulations were performed to study the effect of mineral content on the microextension of the hydraulic fracture, extension behavior, and evolution law of shale. The results showed that changes in the mineral content resulted in changes in the forces between molecules within the minerals, which, in turn, affected the shale's brittleness. The percentages of brittle mineral content in the Long I, II, and III reservoir sections are 60.37, 47.60, and 53.56%, respectively. The fracture initiation pressures of the three reservoirs were 29.22, 31.42, and 30.22 MPa, respectively, and a linear correlation was found between the fracture initiation pressures and the brittle mineral contents of the reservoir sections. An increase in the reservoirs' percentage of brittle mineral content facilitated the fracture initiation, with a corresponding gradual decrease in the resistance to fracture initiation. The pore pressures of the fractures in the three reservoirs after fracture initiation were 0.90, 1.18, and 1.00 MPa, respectively. The larger the percentage of brittle minerals was, the lower was the fracture pore pressure. The greater the length, number, area, and width of the cracks were, the more likely they were to form longer and wider cracks. Hence, reservoirs with a high percentage of brittle minerals should be prioritized as the target formations for hydraulic fracturing operations. The results of this study reveal how the mineral content affects the extension of microscopic hydraulic fractures in shale reservoirs. As such, this work can provide a theoretical basis for rationally selecting a hydraulic fracturing operation layer in shale gas reservoirs.



## 1. INTRODUCTION

Several countries have closely monitored shale gas as a special oil and gas energy. It is clean, environmentally friendly, self-generating, and self-storing.<sup>1</sup> Hydraulic fracturing is used to increase shale gas production capacity, and it involves modifying shale reservoirs.<sup>2</sup> In this method, an ideal target layer must be selected. This paper explores the effects of a shale reservoir's structure on fracture expansion on a microscale during hydraulic fracturing. It describes the expansion and evolution laws of microscopic hydraulic fractures and provides a theoretical basis for selecting target layers for hydraulic fracturing for shale.

The brittleness of the rock considerably affects the ease of hydraulic fracturing and fracture morphology. Brittleness evaluation and fractured segment selection have been primarily based on mineral composition or elastic parameters.<sup>3</sup> The mineral composition of shale is a crucial part of its microstructure, and most scholars consider clay minerals as ductile minerals and minerals with a high Young's modulus and low Poisson's ratio (such as quartz, pyrite, and calcite, etc.) as brittle minerals.<sup>4,5</sup> The microstructure of shale is a microscopic characterization of a shale reservoir's properties. Guo et al.<sup>6</sup>

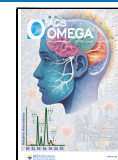
and Liu et al.<sup>7</sup> analyzed the effects of mineral composition and pore microstructure on the elastic properties of a rock mass. Shi et al.,<sup>8</sup> Wang et al.,<sup>9</sup> and Aoudia et al.<sup>10</sup> found that the elastic properties of shale primarily depend on its clay and quartz mineral content. Liu et al.,<sup>11</sup> Li et al.,<sup>12</sup> Dou and Wang,<sup>13</sup> and Gong et al.<sup>14</sup> investigated the effect of mineral inhomogeneity on fracture extension. Zhou et al.<sup>15</sup> and Fazeli et al.<sup>16</sup> investigated the effect of brittle minerals and clay minerals on the pore structure of shale microscopically. Song et al.,<sup>17</sup> Yang et al.,<sup>18</sup> and Liu et al.<sup>19</sup> reconstructed generic and easy-to-implement pore-scale models by micro-CT imaging. The results of He et al.<sup>20</sup> and Li et al.<sup>21</sup> indicated that microcracks were observed to generally propagate along the boundaries of hard

Received: January 25, 2024

Revised: July 9, 2024

Accepted: July 10, 2024

Published: July 20, 2024



mineral particles and soft organic matter. Elsworth et al.<sup>22</sup> found that the predominance of small grains or point contacts of quartz minerals promotes brittle damage and that fracture morphology, fill length, and extent affect shale deformability. Dou et al.,<sup>23</sup> Sarkar et al.,<sup>24</sup> and Huang et al.<sup>25</sup> studied the mechanical properties of shale reservoir minerals found a high correlation among the occurrence, continuity, and mineralogical filling of fracture morphology patterns.

The effectiveness of hydraulic fracturing in shale reservoirs depends on many factors,<sup>26–28</sup> such as mineral fraction content, stratigraphy, and natural fractures. Among these factors, the mineral fraction content plays a key role in determining the properties of a shale reservoir and the hydraulic fracture extension. Kusuma et al.<sup>29</sup> and Ferguson et al.<sup>30</sup> observed production anomalies after hydraulic fracture stimulations, and the clay release caused by hydraulic fracturing increased the effective porosity and permeability. Vahab et al.<sup>31</sup> and Taleghani et al.<sup>32</sup> used numerical simulations to study the evolution of hydraulically driven fractures in naturally layered and fractured media. Jiang et al.<sup>33</sup> used the extended finite element method to investigate the fracture extension law of hydraulic fracturing under the influence of different far-field stresses, fracture and hole leakage behaviors, and other factors. Moghaddam and Golshani<sup>34</sup> and Benouadah et al.<sup>35</sup> investigated the effect of structural anisotropy and anisotropic toughness conditions on the hydraulic fracturing process through true triaxial hydraulic fracturing experiments and numerical simulations, respectively. Zhao et al.<sup>36</sup> found that the morphological evolution of fracturing cracks became more prominent as the effective normal stress increased, which was related to the change in the effective contact area. Dontsov et al.<sup>37</sup> and Wu et al.<sup>38</sup> used numerical simulations to investigate the effect of stiffness and toughness ratios on the growth of hydraulic fracture heights and found that bending extensions were more pronounced when inhomogeneous distributions of mechanical parameters of the rock mass were considered. Deng et al.<sup>39</sup> investigated the effect of different elastic moduli and stress differences on the interaction of hydraulic fractures with laminated weak interfaces using a discrete fracture model and an extended finite element method. Evidently, studies on hydraulic fracture extension have mostly focused on the macro scale; no studies have investigated the influence of a shale reservoir's structure on microhydraulic fracture extension and evolution.

In this study, brittle minerals, such as quartz, calcite, feldspar, and pyrite, in shale reservoirs were investigated. We developed a geometric model for the stochastic distribution of shale gas reservoir minerals on the microscopic scale. A discrete solid grid was delineated and embedded with zero-thickness cohesive cells to simulate shale hydraulic fracturing. We investigated the mechanical properties' variability of different mineral components and the influence of mineral content on the fracture extension pattern of hydraulic fracturing in shale gas reservoirs. The results of this study clarify the expansion and evolution of microscopic hydraulic fractures.

## 2. SHALE HYDRAULIC FRACTURING FLUID–SOLID COUPLING THEORY

**2.1. Rock Fluid–Solid Coupling Model.** A fracturing fluid is injected to induce the initiation and extension of cracks in a rock. For simplicity, the finite element model developed in this study satisfies the following basic assumptions:

- (1) The formation is a homogeneous isotropic pore material, and the rock particles are incompressible.
- (2) The fluid fills the cracks without considering the fluid hysteresis effect.
- (3) The fluid is assumed to be an incompressible Newtonian fluid.
- (4) The crack extension is a plane-strain quasistatic process, neglecting the effect of inertial forces.

The equilibrium equation for the solid skeleton in porous media in the current configuration is defined as

$$\int_V (\bar{\sigma} - p_w \mathbf{I}) \delta \boldsymbol{\varepsilon} dV = \int_S \mathbf{t} \delta \mathbf{v} dS + \int_V \mathbf{f} \delta \mathbf{v} dV \quad (1)$$

where  $\bar{\sigma}$  is the effective stress matrix,  $p_w$  is the pore pressure,  $\delta \boldsymbol{\varepsilon}$  is the imaginary strain rate matrix,  $\mathbf{t}$  is the surface force matrix,  $\mathbf{f}$  is the body force matrix, and  $\delta \mathbf{v}$  is the imaginary velocity matrix.

The effective stress matrix can be expressed as

$$\bar{\sigma} = D \boldsymbol{\varepsilon} + \frac{Dm}{3K_g} p_w - \frac{Dm}{3K_g} p_w^0 + \bar{\sigma}_0 \quad (2)$$

where  $D$  is the elastic–plastic stiffness matrix,  $\boldsymbol{\varepsilon}$  is the strain matrix,  $K_g$  is the bulk modulus of the solid skeleton part of the porous medium,  $p_w^0$  is the initial pore pressure of the fluid, and  $\bar{\sigma}_0$  is the initial effective ground stress matrix.

The continuity equation for a percolating fluid is defined as

$$\frac{1}{J} \frac{\partial}{\partial t} (J \rho_w n_w) + \frac{\partial}{\partial \mathbf{x}} (\rho_w n_w \boldsymbol{\nu}_w) = 0 \quad (3)$$

where  $J$  is the volume change ratio of porous media,  $\rho_w$  is the fluid density,  $n_w$  is the pore ratio,  $\mathbf{x}$  is the space vector, and  $\boldsymbol{\nu}_w$  is the fluid percolation velocity.

The fluid flow in porous media obeys Darcy's law:

$$\boldsymbol{\nu}_w = -\frac{1}{n_w g \rho_w} \mathbf{k} \left( \frac{\partial p_w}{\partial \mathbf{x}} - \rho_w \mathbf{g} \right) \quad (4)$$

where  $\mathbf{k}$  is the permeability matrix and  $\mathbf{g}$  is the gravitational acceleration vector.

**2.2. Zero-Thickness Cohesive Cell.** The traction–separation criterion for unit stiffness degradation<sup>40</sup> and the maximum nominal stress criterion were used as damage criteria. The fracture initiation and extension during hydraulic fracturing were simulated, and the flow of fracturing fluid followed the fluid flow criterion.<sup>41,42</sup>

(1) Traction–separation criterion

In Figure 1,  $\delta_m^f$  is the effective displacement at complete damage,  $\delta_m^0$  is the effective displacement relative to the

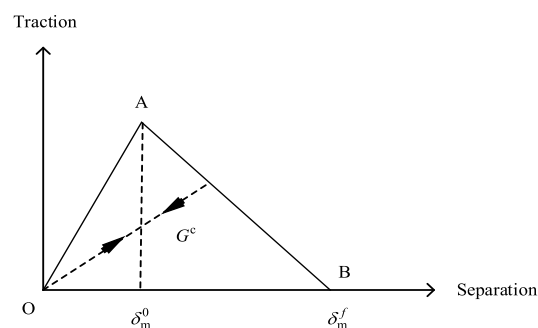
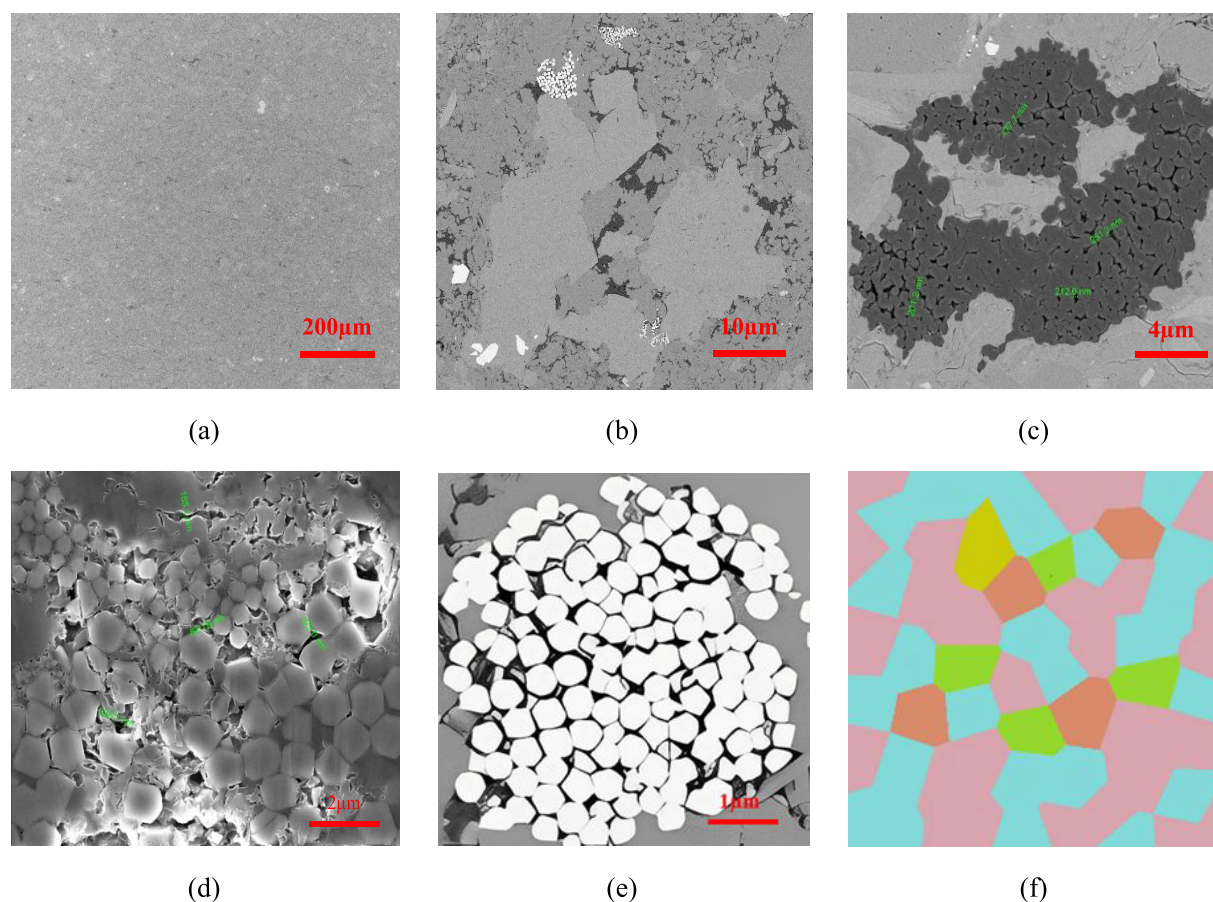


Figure 1. Traction–separation constitutive relationship.



**Figure 2.** (a–f) Microscopic mineral structure of shale.

beginning of the damage, and  $G^c$  is the total energy consumed because of the damage.

As shown in Figure 1, the intrinsic relationship of the cohesive unit is linearly elastic until damage occurs (OA segment). When the stress to which the unit is subjected reaches the maximum stress criterion (AB section), the stiffness of the unit gradually decreases until the unit completely loses its load-bearing capacity.

#### (2) Maximum nominal stress criterion

The maximum nominal stress criterion assumes that the cohesive unit is damaged when the stresses sustained in a direction reach the critical stress, and it is expressed as

$$\max \left\{ \frac{\langle \sigma_n \rangle}{\sigma_n^0}, \frac{\sigma_s}{\sigma_s^0}, \frac{\sigma_t}{\sigma_t^0} \right\} = 1 \quad (5)$$

where  $\sigma_n^0$  is the critical value of the normal stress of the cohesive unit, that is, the tensile strength of the rock reservoir;  $\sigma_s^0$  and  $\sigma_t^0$  are the critical stress in two shear directions, that is, the shear strength of the rock (for anisotropic materials, the shear strength may differ in different tangential directions); and  $\langle \rangle$  indicates that the cohesive unit is not damaged when subjected to a compressive stress.

### 3. NUMERICAL MODELING

**3.1. Shale Microstructure Model.** The shale considered in this study was that of the Longmaxi Formation in the Changning area of the Sichuan Basin. The geotectonic structure of the Changning shale gas exploration block is in the low-steep folded zone in the south of the Sichuan Basin. The main tectonic body

of the study area is in the Changning single-box, long-axis back-slope tectonic belt. The axis of the main tectonic structure of the Changning back-slope is oriented in the NWW-SEE direction, and it extends from the south of Gao County in the west to Xuyong County in the east, disappearing into the Xuyong tectonic structure. The two flanks of the back-slope are asymmetrical, with a steep northern flank and eastern end, as well as a slow southern flank and western end (40–60°), indicating a pattern of a wide east and a narrow west. The strata exposed in the shaft are Lower Ordovician, and the Longmaxi Formation strata are denuded.<sup>43</sup> The Longmaxi Formation shale is widely developed in the Early Silurian Middle and Upper Yangzi. The black shale of the Longmaxi Formation has a thickness of approximately 100–170 m and is mainly distributed in the lower part of the formation. The mineral composition primarily comprises quartz, clay minerals, calcite, feldspar, dolomite, and pyrite. Their approximate mass fractions are as follows: quartz, 31.37%; calcite, 15.66%; dolomite, 3.41%; feldspar, 5.79%; clay mineral, 45.62%; pyrite, 0.99%; and TOC, 1.43%. The mineral content of the Long I section in the Longmaxi Formation shale reservoir is mainly quartz and clay, whereas that of the Long II and Long III sections is mainly quartz, calcite, and clay. The ease of rock fracturing and the morphology of the fractured joints mainly depend on the rock brittleness characteristics. The more brittle the rock is, the more effective is its fracturing. However, no reliable conclusion has been drawn from the research on and evaluation of shale brittleness characterization. Moreover, the brittleness index calculation and brittleness characterization of shale are mainly

based on the mineral composition or elasticity parameters. Currently, commonly used methods for characterizing the fracture-creation capacity of hydraulic fracturing include the mineral brittleness index method and the elastic parameter brittleness index method. As quartz is the main brittle mineral, a proportion of its content can be used to characterize the shale brittleness. In addition, field results have shown that Young's modulus reflects the ability of shale to sustain fractures and that shale with high Young's modulus and low Poisson's ratio is more brittle.<sup>4,5</sup> The high calcium content and pyrite development in the mineral composition of the marine shale in southern China indicate that quartz, calcite, feldspar, dolomite, pyrite, and other minerals have a high content and large regional variations, with obvious "high Young's modulus and low Poisson's ratio" characteristics, as well as the highest degree of brittleness.

Figure 2a,b,e and c,d show the microscopic grain structure of shale observed using field emission scanning electron microscopy and focused ion beam scanning electron microscopy, respectively. We randomly selected the microstructure of shale from different regions and sizes. Figure 2a shows a full view of the shale samples and reveals that organic matter and pyrite are well developed in the Longmaxi Formation shale. Figure 2b shows that the shale matrix is mixed with various minerals; small pieces of organic matter are denser, and tiny micropores are visible. Irregular organic matter pores within 300 nm develop within some of the organic matter, as shown in Figure 2c. Dense pyrite particles and intergranular pores with irregularly distributed particle morphology and pore sizes less than 300 nm are observed in both Figure 2d,e. Figure 2f shows an approximation of the micrograin structure. According to Figure 2d,e, the mineral grains in the shale tend to be densely packed and randomly distributed in an irregular pattern. Therefore, the material region can be discretized into irregular polygonal grain systems.

We developed a geometric model based on a previous study<sup>3</sup> for the random distribution of mineral fractions in the outcrop shales of the Longmaxi Formation in the Sichuan Basin. The random generation of polygonal mineral particles was based on Monte Carlo random distribution and the Tyson polygon. The geometric model was generated through the following steps: (1) Determination of the area of mineral components' generation. (2) Determination of the percentage of mineral components as a condition for determining the cessation of polygonal structure generation. (3) Generation of random numbers to determine the mineral particles' shapes and sizes. The Voronoi diagram's partition space is based on the following principle: (i) a random distribution of discrete points in the space to be partitioned; (ii) the intersection of the perpendicular bisectors of the lines connecting adjacent discrete points forms the vertices of the polygon surrounding the discrete points; (iii) every trio of adjacent vertices forms a Delaunay triangle, and the Tyson polygon is obtained by connecting the outer circle centers of all adjacent triangles at each discrete point. (4) Determination of the boundary conditions and distance between polygons to ensure that the generated polygonal mineral particles are within a defined area and that adjacent polygonal mineral particles are connected to each other. A secondary stochastic distribution model of mineral fractions in different shale reservoirs was developed using the Python programming language. Table 1 lists the mineral fraction contents of the shale reservoirs in the Longmaxi Formation's Long I, II, and III sections in the Sichuan Basin.

**Table 1. Mineral Content of Different Reservoirs**

| mineral content (%) | quartz | feldspar | calcite | pyrite | clay  |
|---------------------|--------|----------|---------|--------|-------|
| Long I section      | 45.57  | 6.71     | 7.02    | 1.43   | 39.27 |
| Long II section     | 24.87  | 4.95     | 16.95   | 0.83   | 52.40 |
| Long III section    | 23.34  | 5.75     | 23.77   | 0.70   | 46.44 |

Scholars disagree on the classification of shale brittle minerals. However, most scholars consider clay minerals as ductile minerals and minerals such as quartz, calcite, and feldspar as brittle minerals. Therefore, in this study, quartz, calcite, feldspar, and pyrite minerals were considered as shale brittle minerals. An analysis of the mineral content of the Longmaxi Formation outcrop shale reservoir in the Sichuan Basin shows that the Long I section shale reservoir has the highest brittle mineral content of 60.73% followed by the Long III section shale reservoir at 53.56% and the Long II section shale reservoir at 47.60%.

Figure 3 shows a  $1 \times 1$  mm microstructural model of the shale reservoir. The mineral contents are presented in Table 1, and the mineral fractions are clay, quartz, calcite, pyrite, and five important minerals of feldspar. The mineral particle size was in the range of 80–130  $\mu\text{m}$ . For the discrete solid meshing of the mineral geometry model, a Python program was used to perform the batch insertion of zero-thickness cohesive cells between solid discrete meshes.

**3.2. Boundary Conditions.** Shale hydraulic fracturing is a fluid–solid coupling process, which comprises three phases: initial ground stress balance, fracturing fluid injection, and fracture extension phases. For the stress boundary condition in this study, the displacement in the  $x$  and  $y$  directions was 0; the initial pore pressure was 0 for the seepage boundary condition. A point at the mineral boundary near the center of the geometric model was selected as the shot hole for hydraulic fracturing. The injection direction was along the mineral boundary, and P in Figure 4 indicates the initial position of the fracturing fluid injection. The meshing was performed using four-node-plane strain quadrilateral cells, bilinear displacement, and bilinear pore pressure.

**3.3. Model Parameters.** Model parameter selection is crucial for successful numerical simulations. Prior to the numerical simulation, the stress–strain curves and tensile strength of the shale were obtained through uniaxial compression experiments of standard specimens and Brazilian splitting experiments. On this basis, the individual parameters were continuously adjusted for trial calculations. The calculated parameters of the numerical model were obtained when the stress–strain curves of the uniaxial compression numerical tests coincided with the results of the uniaxial compression physical experiment<sup>44</sup> (Figure 5). Thus, the minimum horizontal principal stress of the numerical model was 8 MPa, whereas the maximum horizontal principal stress was 10 MPa. The porosity was 4.8%, stiffness was 6 GPa, and fracturing fluid discharge was 0.001  $\text{m}^3/\text{s}$ . The fracturing fluid viscosity was 0.001 Pa·s, permeability was  $1 \times 10^{-7} \mu\text{m}^2$ , and tensile strength was 5.96 MPa.

The initial time increment step was 0.01 s, and the fracturing fluid injection time was 60 s. The material parameters of shale reservoir minerals<sup>3</sup> are presented in Table 2.

## 4. NUMERICAL SIMULATION OF SHALE HYDRAULIC FRACTURE EXTENSION AT THE MICROSCALE

### 4.1. Crack Initiation and Extension Process Analysis.

Figure 6a illustrates the initiation and extension of fractures in

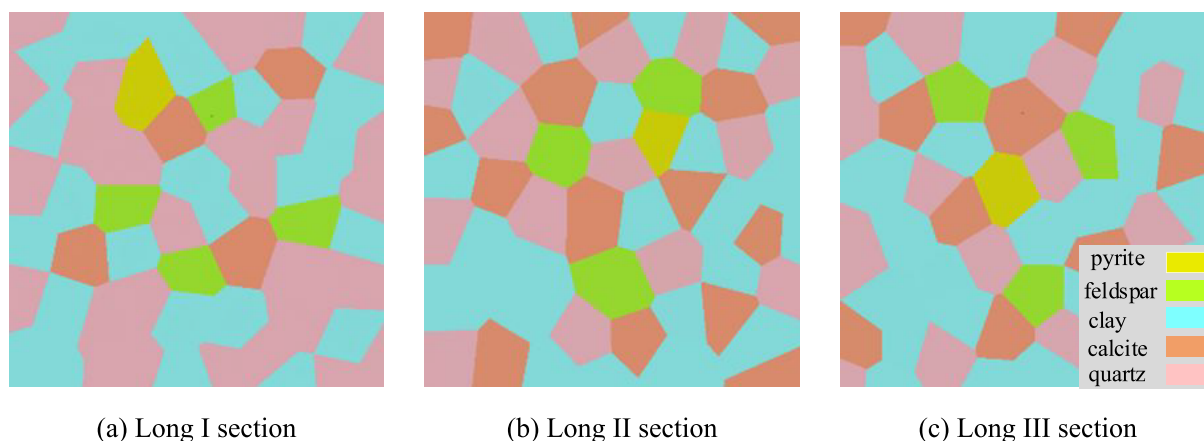


Figure 3. Microgeometric distribution model of shale from different reservoirs.

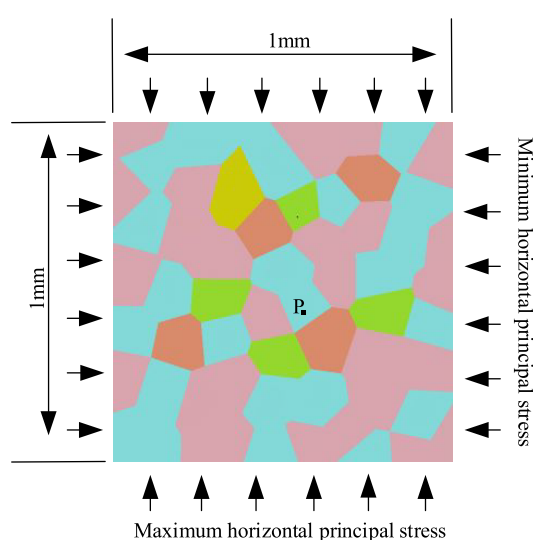


Figure 4. Two-dimensional plane strain model.

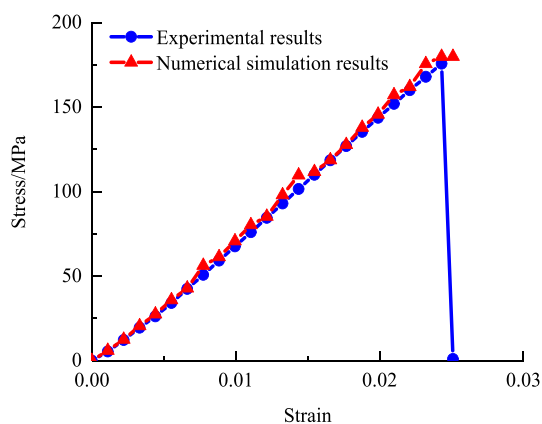


Figure 5. Comparison of stress–strain curves between physical experiment and numerical simulation.

the shale reservoir in the Long I section. After the fracturing fluid was injected, the fracture formation started at an initiation pressure of 29.22 MPa. The effective stress increased and then decreased as the cracks extended, finally settling at 18.16 MPa. The pore pressure increased continuously as crack initiation and extension continued, and the maximum pore pressure was 0.90

Table 2. Material Parameters of Minerals

| minerals | elastic modulus (GPa) | Poisson's ratio |
|----------|-----------------------|-----------------|
| quartz   | 95.89                 | 0.07            |
| clay     | 14.68                 | 0.30            |
| calcite  | 79.23                 | 0.31            |
| feldspar | 69.05                 | 0.36            |
| pyrite   | 306.17                | 0.14            |

MPa. The percentage of tensile damage was greater than 96.56%, and the form of damage was tensile damage.

The initiation and extension of fractures in the shale reservoir in the Long II section are illustrated in Figure 6b. After the fracturing fluid was injected, the fracture started to form with an initiation pressure of 31.42 MPa. The effective stress increased continuously with increasing crack initiation and extension, finally settling at 13.67 MPa. The pore pressure increased and then decreased as crack initiation and extension continued, and it gradually increased subsequently, reaching a maximum value of 1.18 MPa. Tensile damage accounted for more than 82.17% of the damage, and the form of damage was mainly tensile damage.

The initiation and extension of fractures in the shale reservoir in the Long III section are illustrated in Figure 6c. After the fracturing fluid was injected, the fracture started to form at an initiation pressure of 30.22 MPa. The effective stress increased and then decreased as the crack continued expanding, stabilizing at a fixed value and then gradually increasing, finally settling at 16.38 MPa. The pore pressure increased continuously as fracture initiation and extension continued, reaching a maximum value of 1.00 MPa. Tensile damage accounted for more than 95.48%, and the damage form was mainly tensile damage.

Figure 6 illustrates the variation of hydraulic fracturing parameters and the percentage of tensile damage for shale reservoirs in the Long I, II, and III sections. Although their mineral contents are different, all sections had similar fracture initiation processes. After the fracturing fluid was injected, the fracture started forming, and the injection pressure suddenly increased. Subsequently, as the fracture expanded, the trend of the shot hole pressure was unchanged across the sections. Overall, the pore pressure increased as fracture initiation and extension continued. However, regarding the mineral content of the shale reservoir in the Long II section, as shown in Figure 6b, the pore pressure increased slowly as fracture initiation and extension continued, and then it fluctuated suddenly and strongly. Subsequently, the concentration gradually increased

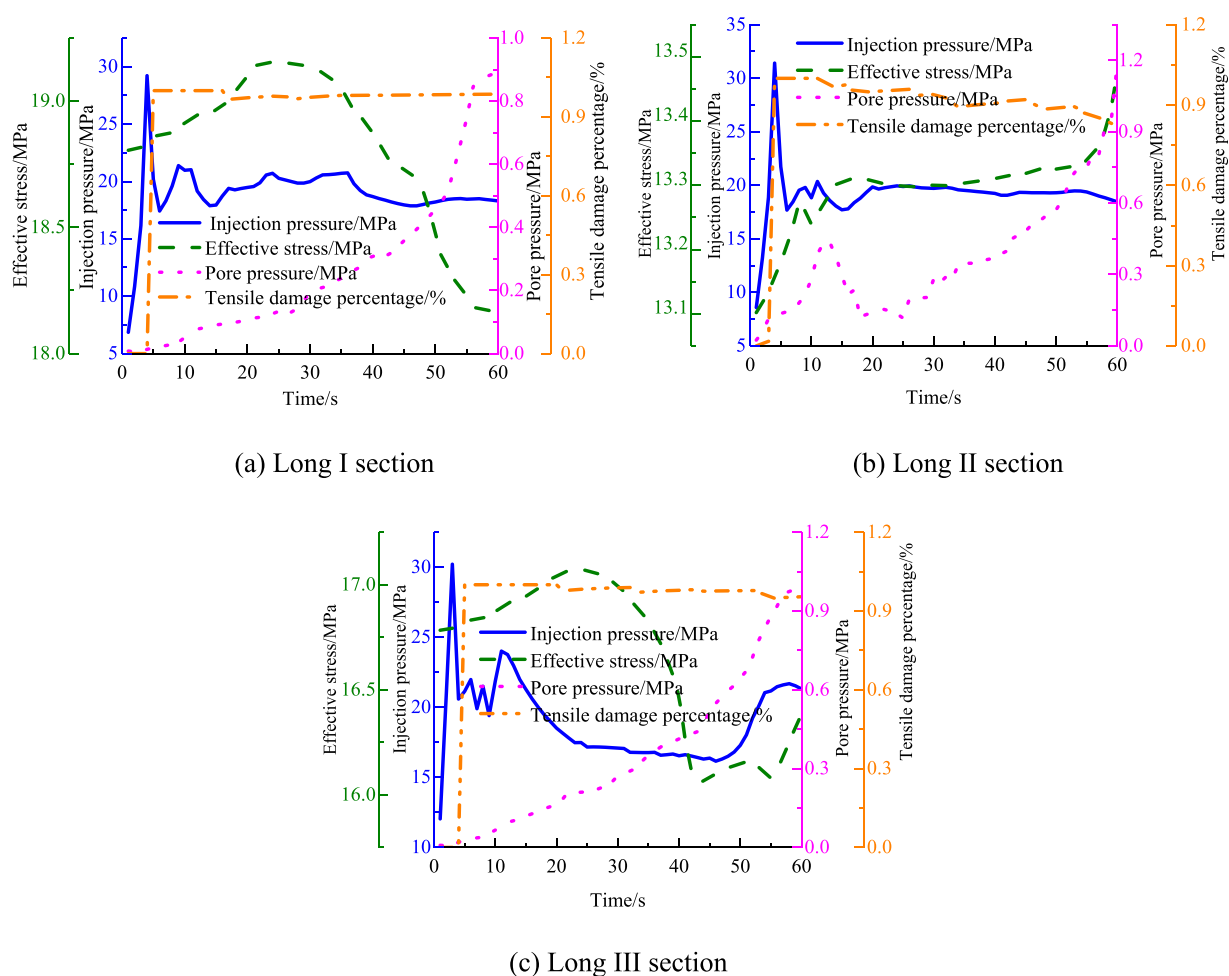


**Figure 6.** Fracturing parameters and tensile damage percentage change pattern.

steadily and finally grew rapidly. Tensile damage accounted for more than 82.17% of the overall damage, and the damage form was mainly tensile damage. The overall trend of the effective stress was an increase followed by a decrease with continuing fracture initiation and extension for the mineral contents of the shale reservoirs in both the Long I and III sections. However, with regard to the mineral content of the shale reservoir in the Long II section, the effective stress increased continuously as fracture initiation and extension continued.

**4.2. Crack Extension Pattern Analysis.** (1) Crack extension final form

Figure 7 shows the final extension pattern of hydraulic fractures in the Long I, II, and III shale reservoirs after injection of the fracturing fluid. The upper and lower flanks of the hydraulic fractures in the shale reservoir in the Long I section (Figure 7a) were first extended along the mineral boundary. Both the upper flank fracture and the lower flank fracture passed through the clay minerals. The upper flank fracture extension stopped in calcite minerals, whereas the lower flank fracture extension stopped in quartz minerals. The upper flank of the hydraulic fracture in the shale reservoir of the Long II section (Figure 7b) passed through the pyrite mineral, whereas the fracture extension stopped at the mineral boundary. The lower flank cracked through the clay minerals and finally rested in the feldspar minerals. The hydraulic upper flank fractures and lower flank fracture extensions of the shale reservoir in the Long III section (Figure 7c) both stopped in the mineral. The upper flank

fracture passed through the pyrite mineral and finally stopped in the calcite mineral. The lower flank cracked through the clay minerals and finally rested in the feldspar minerals. The results depicted in Figures 7 and 8 show that two types of interactions occurred between the fracture extension and the mineral interface. First, the extension occurred along the mineral boundary; second, the extension occurred through the mineral boundary and into the mineral. This phenomenon mainly occurred because the stress field around the cracks changed constantly during the crack extension. Moreover, as the brittle mineral content increased, crack initiation and extension became easier. However, overall, the cracks expanded in the direction of parallel maximum principal stress.

(2) Crack morphology parameters

The extension patterns of fractures in the shale reservoir in the Long I section are illustrated in Figure 8a. The trends of the crack length, rupture unit, and area were generally consistent. The maximum crack width was at the initial position (as shown in Figure 7a), and the maximum value of the crack width was  $2.056 \mu\text{m}$ . The maximum value of the crack length was 0.36 mm; the rupture unit of cracks was 94, and the crack area was  $13.78 \mu\text{m}^2$ .

The extension pattern of the fractures in the shale reservoir in the Long II section is illustrated in Figure 8b. The trends of the crack length, rupture unit, and area were generally consistent. The maximum crack width was at the initial position (as shown in Figure 7b), and the maximum value of the crack width was

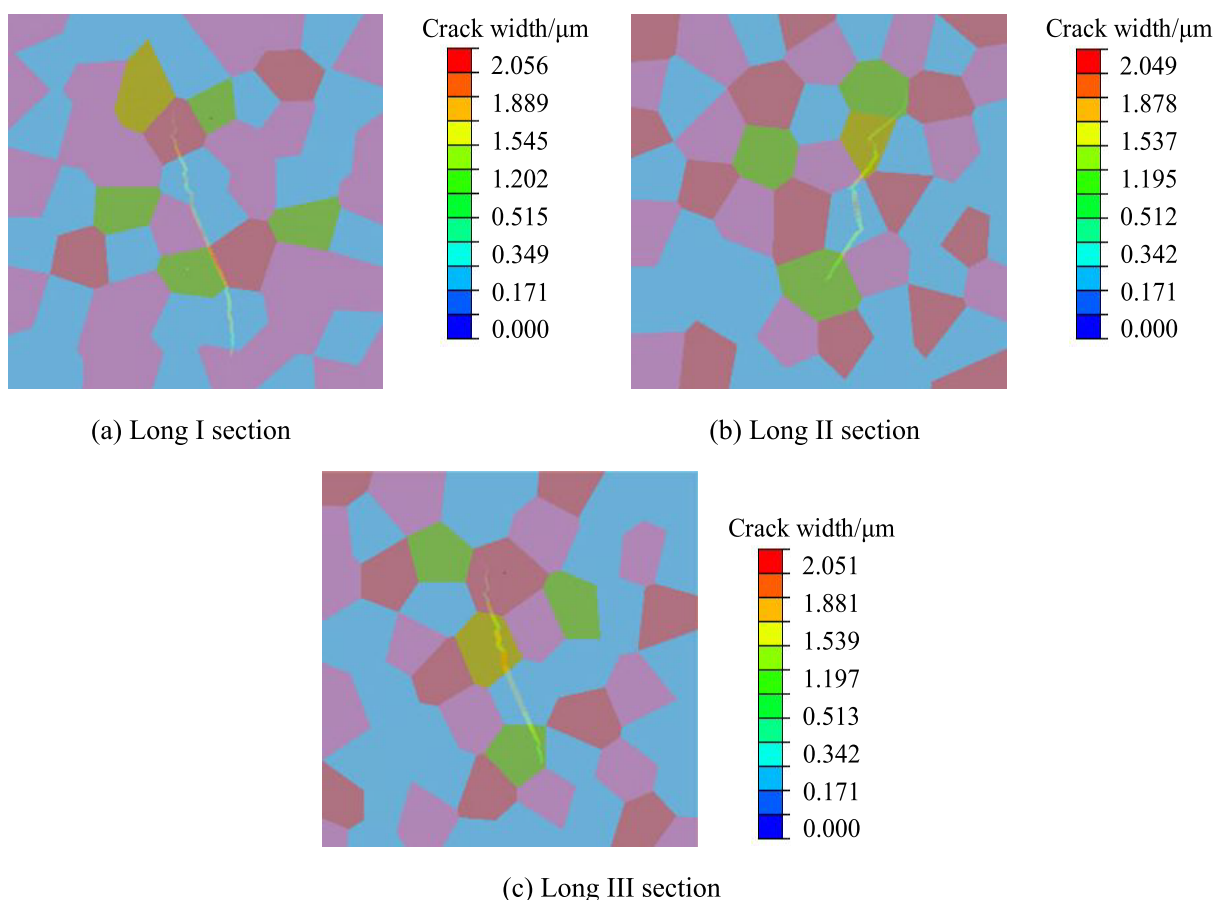


**Figure 7.** Fracture extension results for different shale reservoirs.

2.049  $\mu\text{m}$ . The maximum value of the crack length was 0.29 mm; the rupture unit of cracks was 83, and the crack area was 6.00  $\mu\text{m}^2$ .

The extension pattern of fractures in the shale reservoir in the Long III section is illustrated in Figure 8c. The trends of the crack length, rupture unit, and area were generally consistent. The maximum crack width was at the initial position (as shown in Figure 7c), and the maximum value of the crack width was 2.051  $\mu\text{m}$ . The maximum value of the crack length was 0.33 mm; the rupture unit of cracks was 84, and the crack area was 9.25  $\mu\text{m}^2$ .

Figure 8 illustrates the variation of hydraulic fracture morphology in the Long I, II, and III sections. Although the mineral contents differed across the sections, the overall trends of the fracture length, rupture unit, area, and maximum fracture width variation were generally consistent. All of the quantities increased as crack initiation and extension continued, and the maximum crack width was at the initial position (e.g., Figure 7). However, regarding the mineral content of the shale reservoir in the Long II section, as shown in Figure 8b, the maximum fracture width fluctuated slightly more. As the fracturing fluid was injected, the maximum fracture width increased slowly and then rapidly before gradually stabilizing. However, regarding the mineral content of the shale reservoir in the Long III section, as shown in Figure 8c, the variation trend of the fracture length was slightly different: as the fracturing fluid was injected, the fracture length first remained stable, and then it increased suddenly before finally increasing slowly. Regarding the mineral content of the shale reservoirs in the Long I and II sections, the rupture

unit of fractures first remained stable and constant before increasing abruptly and finally stabilizing gradually. However, regarding the mineral content of the shale reservoir in the Long III section, the rupture unit of fractures showed the trend of a gradual increase as the fracturing fluid injection continued.

## 5. EFFECT OF MINERAL CONTENT ON CRACK INITIATION AND EXTENSION PATTERNS

**5.1. Crack Initiation Behavior under Different Mineral Contents.** Figure 9 illustrates the variation pattern of the effective stress and pore pressure under different mineral contents. As the mineral content changed, the forces between molecules within the minerals changed accordingly, which, in turn, changed the brittleness of the shale. The Long I section shale reservoir had the highest brittle mineral content of 60.37%. The Long II section shale reservoir had the least amount of brittle minerals at 47.60%. Therefore, the fracture initiation pressure value for the Long I section of the shale reservoir was the smallest at 29.22 MPa. The Long II section shale reservoir had the largest fracture initiation pressure at 31.42 MPa. There is a linear relationship between the fracture initiation pressure and brittle mineral content of the reservoir. As the brittle mineral content increased, crack initiation became easier. The crack initiation pressure decreased from 31.42 to 29.22 MPa, and the resistance to crack initiation gradually decreased. As the formation was easier to fracture, the fracturing fluid was dispersed within the fracture, causing the pore pressure inside the fracture to decrease continuously from 1.18 to 0.90 MPa. In turn, the effective stress in the cracks increased gradually from

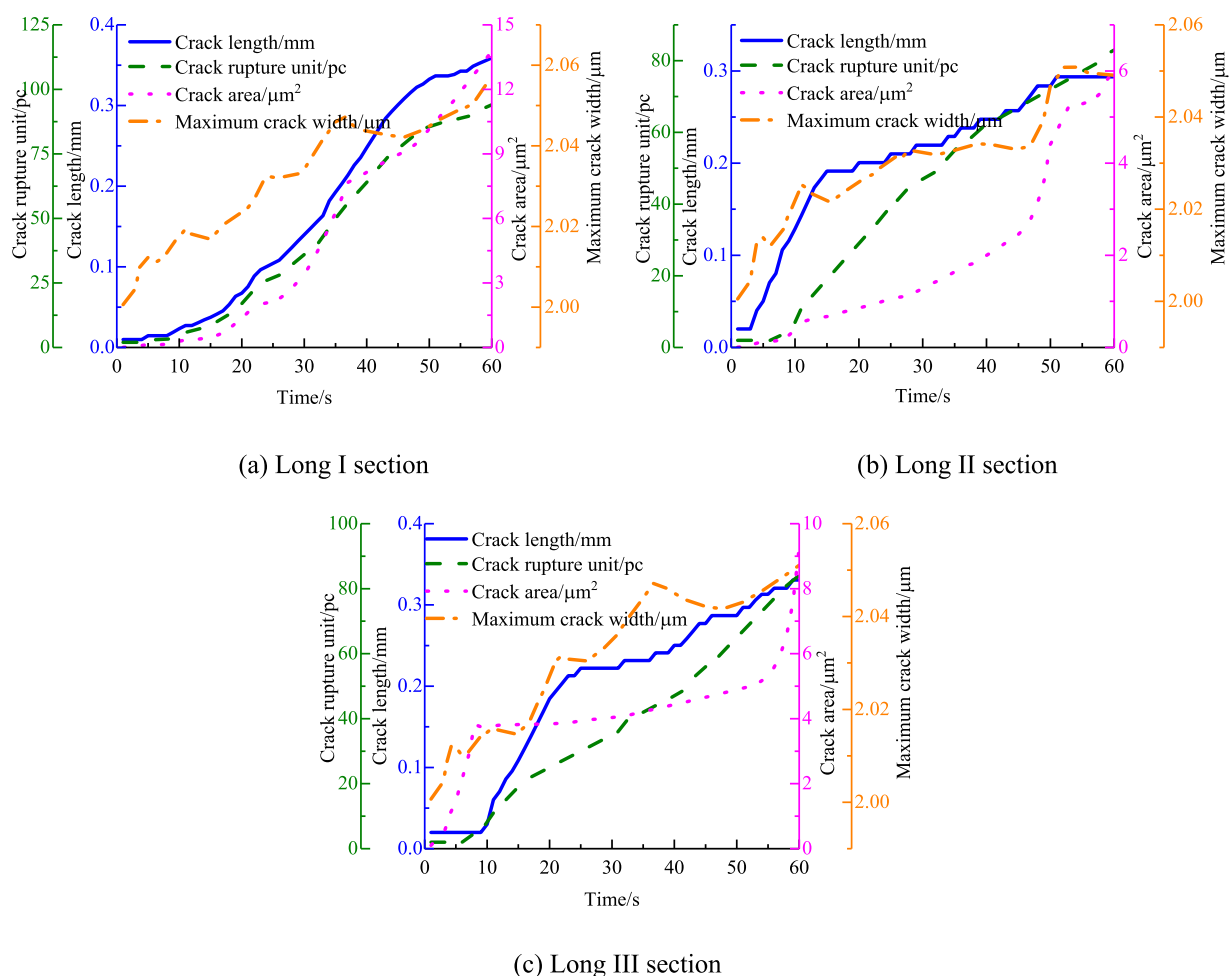


Figure 8. Variation pattern of fracture morphology parameters.

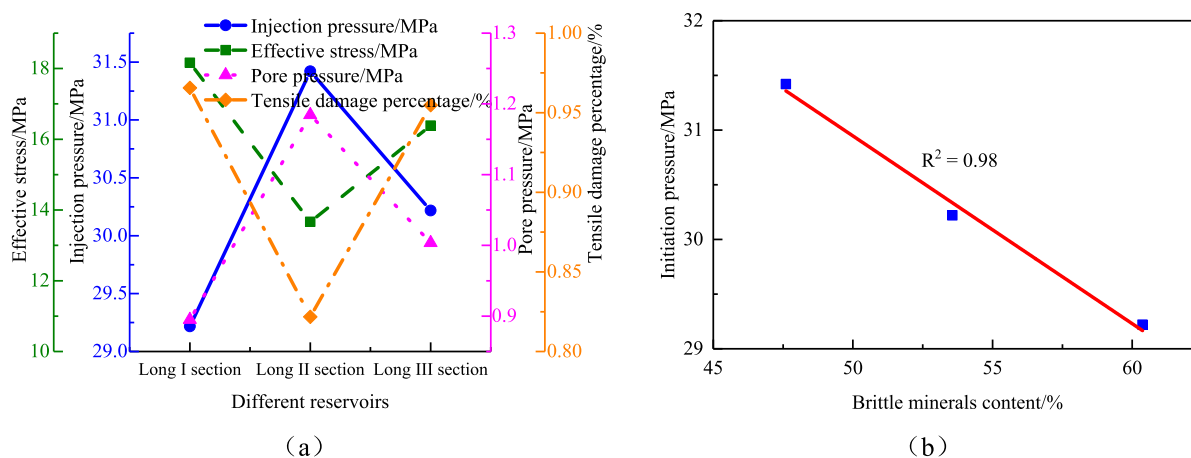
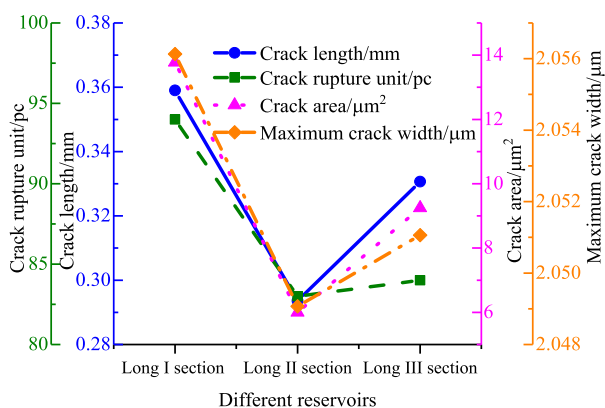


Figure 9. Variation of fracturing parameters and tensile damage percentage under different mineral contents.

10.91 to 18.16 MPa. The crack extension criterion is the maximum stress criterion; when the stress reached the tensile strength, the crack started to form. The crack damage form was predominantly tensile damage, and it mainly formed open cracks.

**5.2. Crack Extension Pattern under Different Mineral Contents.** The crack length, rupture unit, and area as well as the maximum crack width varied with mineral content when the crack extension stopped, as shown in Figure 10. The maximum

crack width was closer with increasing brittle mineral content, increasing from 2.049 to 2.056  $\mu\text{m}$ . The trends in the rupture unit, length, and area of cracks, as well as the maximum crack width, were generally consistent. That is, the rupture unit, length, and area of cracks gradually increased with an increase in brittle mineral content. However, the variation in the rupture unit and area of cracks gradually increased, and the variation in the crack length was generally stable. As the volume of fracturing fluid injected at the same time was the same for all cases, the



**Figure 10.** Variation pattern of fracture morphology parameters with different mineral contents.

volume of fracturing fluid in the fracture was generally unchanged after removing a small amount of fracturing fluid filtered out of the formation. For two-dimensional fractures, the fracturing fluid volume is determined by both the length and width of the fracture. The area, length, and rupture unit of the cracks gradually increased as the crack width varied less. Meanwhile, as the Long I section shale reservoir has the most brittle minerals and the Long II section shale reservoir has the least brittle minerals, the former had the largest rupture unit, length, and area of fractures as well as the maximum fracture width value and the best fracture extension. Therefore, the Long II section of the shale reservoir had the smallest fracture rupture unit, length, area, and maximum fracture width values, as well as the worst fracture extension.

**5.3. Effect of Mineral Content on Fracturing Effect.** The Long I section of the shale reservoir had the lowest fracture initiation pressure, the highest effective stress, the lowest pore pressure, the longest fracture length, the largest rupture unit of fractures, the largest fracture area, and the largest maximum fracture width. The Long II section had the largest fracture initiation pressure, the smallest effective stress, the largest pore pressure, the shortest fracture length, the smallest rupture unit of fractures, the smallest fracture area, and the smallest maximum fracture width. This result indicates that the variation of the mineral content significantly affects the fracture initiation and extension pattern of shale hydraulic fracturing.

At the microscopic level, the forces between molecules within different mineral boundaries vary with the mineral content. As such, the interfacial interactions between different minerals changes. At the macroscopic level, the shale brittleness increases, whereas the intermolecular forces decrease as the brittle mineral content increases. This phenomenon reduces the cohesion between the mineral components. Consequently, crack initiation is easier, crack initiation pressure is lower, and crack extension is faster, indicating that a higher amount of brittle mineral content promotes fracture modification of shale gas reservoirs.

In summary, with the increase in the brittle mineral content, the crack length and width gradually increased, which was more likely to form long and wide cracks. The amount of change in the crack length was considerably greater than that in the crack width. Although the amount of fracture width variation was small, the effect of fracture width on the fracturing effect based on size was not negligible because the modeling was performed on a microscopic scale. In the use of hydraulic fracturing to improve shale gas production, the length and width of hydraulic

fractures are important factors that affect shale gas production. The longer the fracture length is and the wider the width is, the larger is the reservoir's hydraulic fracturing area, which can effectively improve the seepage channel of the reservoir and reduce the difficulty of on-site fracturing construction.

The Long I section shale reservoir had the highest brittle mineral content, the longest fracture length, the largest fracture width, the largest rupture unit of fractures, and the best fracturing effect. The Long II section shale reservoir had the lowest brittle mineral content, the shortest fracture length, the smallest fracture width, the least rupture unit of fractures, and the worst fracturing effect. Therefore, locations with a high brittle mineral content are preferable for hydraulic fracturing operations in shale gas reservoirs.

## 6. DISCUSSION

Different kinds of minerals or the same minerals with different genesis contribute in different ways to the properties and hydraulic fracturing effects of shale reservoirs because of their different physical properties, endowment states, and output forms. Therefore, the Chongqing area<sup>45,46</sup> is discussed here in comparison with the shale in Changning area. First, the mineral content of the Long I section of the Longmaxi Formation shale reservoir is predominantly quartz and clay minerals, and the contents of quartz and clay minerals are 45.57 and 39.27%, respectively. Both the Long II and III sections are primarily composed of quartz, calcite, and clay minerals. The quartz, calcite, and clay mineral contents of the Long II shale reservoir are 24.87, 16.95, and 52.40%, respectively, whereas those of the shale reservoir of the Long III section are 23.34, 23.77, and 46.44%, respectively. The mineral content of shale reservoirs in Chongqing is mainly composed of quartz, carbonate, and clay minerals, with average contents of 49, 21, and 22%, respectively.

A comparison of the hydraulic fracture extensions under the influence of the mineral content shows that the maximum principal stress and mineral inhomogeneity of shale reservoirs in different regions are crucial factors affecting fracture extension. Macroscopically, the maximum principal stress determines the overall hydraulic fracture trend, whereas the mineral inhomogeneity traps hydraulic fractures locally and interferes with the direction of the fracture extension. Meanwhile, mineral nonhomogeneity can cause a nonuniform distribution of stress, leading to a nonsynchronous expansion of hydraulic cracks and indirectly increasing the hydraulic crack complexity. Changes in the characteristics of the pore water pressure can be used to characterize the crack extension indirectly: the greater the fluctuation of the pore water pressure curve is, the more complex is the crack path.

Our comparison of the hydraulic fracture extension in both regions shows that the increase in brittle mineral content increases the brittleness of the shale and affects the hydraulic fracture extension. When a hydraulic fracture encounters a brittle mineral, the hydraulic fracture expands through and around the brittle mineral. When brittle minerals are bypassed, hydraulic fractures can turn or form branching fractures. The larger the volume fraction of brittle minerals is, the greater is the extent of the impact of hydraulic fracture extension.

## 7. CONCLUSIONS

A shale microstructural model was developed using a Monte Carlo random distribution and Tyson polygon. The fracture extension in shale reservoirs was modeled for different mineral

contents. Then, the fracture extension behavior of the shale reservoirs' fracturing under different mineral contents was determined. The main conclusions are as follows:

1. A microstructural model of shale reservoirs was developed. A zero-thickness cohesive unit was embedded within the solid unit to construct a coupled fluid–solid model for shale reservoir fracturing.
2. The mineral content of the Long I section in the Longmaxi Formation shale reservoir is predominantly quartz and clay. The Long II section is predominantly quartz, calcite, and clay. The Long III section is predominantly quartz, calcite, and clay. The brittle mineral content of the shale reservoir in the Long I section is the largest followed by the Long III section, with the Long II section having the lowest. The opposite is true for the ductile mineral content.
3. The effective stress in the Long I section increased and then decreased as the fracture extension continued during fracturing. The effective stress in the Long II reservoir increased with fracture initiation and extension. The effective stress in the reservoir of the Long III section underwent an increasing–decreasing–stabilizing–unchanging–increasing pattern as the fracture extended. The pore pressures of the three shale reservoirs generally increased gradually, and the damage forms were predominantly tensile damage.
4. Two kinds of interaction existed between fracture extension and mineral interfaces in the fractured shale reservoirs of the Longmaxi Formation. The first was an extension along the mineral boundary, and the second was an extension across the mineral boundary and into the mineral. These interactions were determined by the brittle mineral content and the direction of the maximum principal stress.
5. As the brittle mineral content increased, the cracking pressure and pore pressure gradually decreased, and the effective stress increased. Meanwhile, the length and rupture unit of the cracks as well as the area gradually increased; the width of the cracks gradually increased, facilitating the formation of long and wide cracks. The crack damage form was predominantly tensile damage, and tension-type cracks were mostly formed.

## ■ AUTHOR INFORMATION

### Corresponding Author

**Mengru Hou** – School of Mechanics and Engineering, Liaoning Technical University, Fuxin, Liaoning 123000, China; [orcid.org/0009-0009-5457-5444](https://orcid.org/0009-0009-5457-5444); Email: [hmr2022114@163.com](mailto:hmr2022114@163.com)

### Authors

**Weiji Sun** – School of Mechanics and Engineering, Liaoning Technical University, Fuxin, Liaoning 123000, China

**Bing Liang** – School of Mechanics and Engineering, Liaoning Technical University, Fuxin, Liaoning 123000, China

**Qi Liu** – School of Mechanics and Engineering, Liaoning Technical University, Fuxin, Liaoning 123000, China; [orcid.org/0000-0001-5621-9798](https://orcid.org/0000-0001-5621-9798)

**Hang Zhao** – School of Architecture and Civil Engineering, Anhui Polytechnic University, Wuhu, Anhui 241000, China

**Jianfeng Hao** – College of Mining, Liaoning Technical University, Fuxin, Liaoning 123000, China; [orcid.org/0000-0001-8726-0646](https://orcid.org/0000-0001-8726-0646)

Complete contact information is available at: <https://pubs.acs.org/10.1021/acsomega.4c00826>

## Notes

The authors declare no competing financial interest.

## ■ ACKNOWLEDGMENTS

This research was supported by the National Science and Technology Major Project of the Ministry of Science and Technology of China (Grant 2017ZX05037001), the Discipline Innovation Team Funding Project of Liaoning Technical University (Grant LNTU20TD-11), and the Joint Open Fund for State Key Laboratories of Liaoning Provincial Science and Technology Plan (Grant 2021KF1304).

## ■ REFERENCES

- (1) He, X.; Wu, J.; Yong, R.; et al. Accumulation conditions and key exploration and development technologies of marine shale gas field in changing-Weiyan block, Sichuan Basin. *Acta Pet. Sin.* **2021**, *42* (2), 259–272.
- (2) Frash, L.-P. Laboratory-scale study of hydraulic fracturing in heterogeneous media for enhanced geothermal systems and general well stimulation. Dissertations & Theses Gradworks, Colorado School of Mines 2014.
- (3) Zhang, C.-C.; Wang, Y.-M.; Dong, D.-Z. Brittleness characteristics of Wufeng-Longmaxi shale in Changning region, Southern Sichuan, China. *Nat. Gas Geosci.* **2016**, *27*, 1629–1639.
- (4) Cao, D.; Han, J.; Xiao, J.; et al. Method for evaluating the brittleness of shale minerals under the constraints of elastic characteristics. *Chin. J. Geophys.* **2023**, *66* (11), 4781–4791.
- (5) Chen, J.; Xiao, X.-M. Mineral composition and brittleness of three sets of Paleozoic organic-rich shales in China South area. *J. China Coal Soc.* **2013**, *38* (5), 822–826.
- (6) Guo, Z.; Li, X. Y.; Liu, C.; Feng, X.; Shen, Y. A shale rock physics model for analysis of brittleness index, mineralogy and porosity in the Barnett Shale. *J. Geophys. Eng.* **2013**, *10*, No. 025006.
- (7) Liu, J.; Ding, W.; Wang, R.; Yang, H.; Wang, X.; Li, A. Correlation analysis of element contents and mechanical characteristics of shale reservoirs: A case study in the Cen'gong block. *South China. Mar Petrol Geol.* **2018**, *91*, 19–28.
- (8) Shi, Z.-s.; Qiu, Z.; Dong, D.-z.; Lu, B.; Liang, P.-p.; Zhang, M.-q. Lamina characteristics of gas-bearing shale fine-grained sediment of the Silurian Longmaxi Formation of Well Wuxi 2 in Sichuan Basin, SW China. *Pet. Explor. Dev.* **2018**, *45*, 358–368.
- (9) Wang, H.-y.; Shi, Z.-s.; Sun, S.-s.; Zhao, Q.; Zhou, T.-q.; Cheng, F.; Bai, W.-h. Microfacies types and distribution of epicontinental shale: A case study of the Wufeng–Longmaxi shale in southern Sichuan Basin. *China. Pet. Explor. Dev.* **2023**, *50*, 57–71.
- (10) Aoudia, K.; Miskimis, J. L.; Harris, N. B.; Mnich, C. A. Statistical Analysis of the Effects of Mineralogy on Rock Mechanical Properties of the Woodford Shale And the Associated Impacts For Hydraulic Fracture Treatment Design. *44th U.S. Rock Mechanics Symposium and 5th U.S.-Canada Rock Mechanics Symposium 2010*
- (11) Liu, X.; Meng, S.-w.; Liang, Z.-z.; Tang, C.-a.; Tao, J.-p.; Tang, J.-z. Microscale crack propagation in shale samples using focused ion beam scanning electron microscopy and three-dimensional numerical modeling. *Pet. Sci.* **2023**, *20*, 1488–1512.
- (12) Li, Q.; Chen, M.; Zhou, Y.; Jin, Y.; Wang, F.-P.; Zhang, R. Rock Mechanical Properties of Shale Gas Reservoir and their Influences on Hydraulic Fracture. *Int. Pet. Technol. Conf.* **2013**, 16580.
- (13) Dou, F.-k.; Wang, J.-g. A numerical investigation for the impacts of shale matrix heterogeneity on hydraulic fracturing with a two-dimensional particle assemblage simulation model. *J. Nat. Gas Sci. Eng.* **2022**, *104*, No. 104678.
- (14) Gong, L.; Wang, J.; Gao, S.; Fu, X.-f.; Liu, B.; Miao, F.-b.; Zhou, X.-p.; Meng, Q.-g. Characterization, controlling factors and evolution of

fracture effectiveness in shale oil reservoirs. *J. Pet. Sci. Eng.* **2021**, *203*, No. 108655.

(15) Zhou, W. D.; Xie, S. Y.; Bao, Z. Y.; Carranza, E. J. M.; Wang, Y.; Tang, M. L. Modeling of the Correlation Between Mineral Size and Shale Pore Structure at Meso- and Macroscales. *Math. Geosci.* **2021**, *54*, 131–150.

(16) Fazeli, H.; Vandeginste, V.; Rabbani, A.; Babaei, M.; Muljadi, B. Pore-Scale Modeling of Fluid–Rock Chemical Interactions in Shale during Hydraulic Fracturing. *Energy Fuels* **2021**, *35*, 10461 DOI: 10.1021/acs.energyfuels.0c02975.

(17) Song, R.; Liu, J.-j.; Cui, M.-m. A new method to reconstruct structured mesh model from micro-computed tomography images of porous media and its application. *Int. J. Heat Mass Transfer* **2017**, *109*, 705–715.

(18) Song, R.; Liu, J.-j.; Yang, C.-h.; Sun, S.-y. Study on the multiphase heat and mass transfer mechanism in the dissociation of methane hydrate in reconstructed real-shape porous sediments. *Energy* **2022**, *254*, No. 124421.

(19) Liu, Q.; Li, J.-L.; Liang, B.; et al. Complex wettability behavior triggering mechanism on imbibition: A model construction and comparative study based on analysis at multiple scales. *Energy* **2023**, *275*, No. 127434.

(20) He, J.; Li, X.; Yin, C.; Zhang, Y.; Lin, C. Propagation and characterization of the micro cracks induced by hydraulic fracturing in shale. *Energy* **2020**, *191*, No. 116449.

(21) Li, Z.; Li, L.; Li, M.; Zhang, L.; Zhang, Z.; Huang, B.; Tang, C. A numerical investigation on the effects of rock brittleness on the hydraulic fractures in the shale reservoir. *J. Nat. Gas Sci. Eng.* **2017**, *22*.

(22) Li, Y.; Chen, J.; Elsworth, D.; Pan, Z.; Ma, X. Nanoscale mechanical property variations concerning mineral composition and contact of marine shale. *Geosci. Front.* **2022**, *13*, No. 101405.

(23) Dou, F.-k.; Hou, P.; Jia, Z.-r.; Wang, C.-g.; Zhao, H.-b.; Wang, Y.-p. Effect of Clay Minerals on Tensile Failure Characteristics of Shale. *ACS Omega*. **2022**, *7*, 24219–24230.

(24) Sarkar, P.; Singh, K. H.; Ghosh, R.; Singh, T. N. Estimation of elastic parameters, mineralogy and pore characteristics of Gondwana shale in Eastern India for evaluation of shale gas potential. *Curr. Sci. India* **2018**, *115*, 710.

(25) Li, L.; Huang, B.; Huang, X.; Wang, M.; Li, X. Tensile and Shear Mechanical Characteristics of Longmaxi Shale Laminae Dependent on the Mineral Composition and Morphology. *Energies* **2020**, *13*, 2977.

(26) Liao, S.-z.; Hu, J.-h.; Zhang, Y. Mechanism of hydraulic fracture vertical propagation in deep shale formation based on elastic–plastic model. *Engineering Fracture Mechanics* **2024**, *295*, No. 109806.

(27) Haddad, M.; Sepehrnoori, K. Simulation of hydraulic fracturing in quasi-brittle shale formations using characterized cohesive layer: Stimulation controlling factors. *Journal of Unconventional Oil and Gas Resources* **2015**, *9*, 65–83.

(28) Fan, C.-H.; Nie, S.; Li, H.; Radwan, A.-E.; Pan, Q.-C.; Shi, X.-C.; Li, J.; Liu, Y.-Y.; Guo, Y. Quantitative prediction and spatial analysis of structural fractures in deep shale gas reservoirs within complex structural zones: A case study of the Longmaxi Formation in the Luzhou area, southern Sichuan Basin. *China. Journal of Asian Earth Sciences* **2024**, *263*, No. 106025.

(29) Kusuma, D.-P.; Haris, A.; Astuti, T.; et al. Shale structure implication in hydraulic fracturing production results: Case study in low resistivity low quality reservoir, offshore North West Java area. *IOP Conference Series Earth and Environmental Science* **2020**, *481*, No. 012055.

(30) Ferguson, B.; Agrawal, V.; Sharma, S.; Hakala, J.-A.; Xiong, W. Effects of Carbonate Minerals on Shale-Hydraulic Fracturing Fluid Interactions in the Marcellus Shale. *FRONTIERS IN EARTH SCIENCE* **2021**, *9*, No. 695978.

(31) Vahab, M.; Hirmand, M.-R.; Jafari, A.; Khalili, N. Numerical analysis of multiple hydro-fracture growth in layered media based on a non-differentiable energy minimization approach. *Eng. Fract. Mech.* **2020**, No. 107361.

(32) Wang, D.; Taleghani, A. D.; Yu, B.; Tan, P. Height Effect on Interactions between the Hydraulic Fracture and Natural Fractures. *Geofluids* **2022**, *2022*, 4642326.

(33) Jiang, T.; Wang, H.; Bian, X.; Wang, D.; Zhou, J.; Yu, B.; Liu, D. Numerical Simulation on Hydrofracture Propagation in Fractured-Vuggy Unconventional Reservoirs. *Geofluids* **2022**, *2022*, 8542453.

(34) Moghaddam, R.-H.; Golshani, A. Experimental study on fracture propagation in anisotropy rock under cyclic hydraulic fracturing. *Eng. Fract. Mech.* **2024**, *295*, No. 109775.

(35) Benouadah, N.; Dontsov, E.; Badrouchi, F.; Rasouli, V. Impact of Toughness Anisotropy on Fracture Initiation Pressure and Morphology in Shale Rocks. *Rock Mechanics and Rock Engineering* **2023**, *56*, 9149–9168.

(36) Zhao, C.; Liu, J.; Dai, H.; Huang, H.; Shi, X. Frictional evolution process and stability properties of Longmaxi shale under fluid injection. *Energy* **2024**, *294*, No. 130910.

(37) Huang, L.-k.; Dontsov, E.; Fu, H.-f.; Lei, Y.; Weng, D.-w.; Zhang, F.-s. Hydraulic fracture height growth in layered rocks: perspective from DEM simulation of different propagation regimes. *International Journal of Solids and Structures* **2022**, *238*, No. 111395.

(38) Wu, M.-y.; Jiang, C.-b.; Song, R.; Liu, J.-j.; Li, M.-h.; Liu, B.; Shi, D.; Zhu, Z.-w.; Deng, B.-z. Comparative Study on Hydraulic Fracturing Using Different Discrete Fracture Network Modeling: Insight from Homogeneous to Heterogeneity Reservoirs. *Engineering Fracture Mechanics* **2023**, *284*, No. 109274.

(39) Deng, Y.-h.; Xia, Y.; Wang, D.; Jin, Y. A study of Hydraulic fracture propagation in laminated shale using extended finite element method. *Computers and Geotechnics* **2024**, *166*, No. 105961.

(40) Wu, Z.; Sun, H.; Wong, L. N. Y. A Cohesive Element-Based Numerical Manifold Method for Hydraulic Fracturing Modelling with Voronoi Grains. *Rock Mech. Rock Eng.* **2019**, *2335*.

(41) Dean, R. H.; Schmidt, J. H. Hydraulic-Fracture Predictions with a Fully Coupled Geomechanical Reservoir Simulator. *Spe. J.* **2009**, *14*, 707–714.

(42) Hagoort, J.; Weatherill, B. D.; Settari, A. Modeling the Propagation of Waterflood-Induced Hydraulic Fractures. *SPE. J.* **1980**, *20*, 293–303.

(43) Zhou, H.; Chen, L.; Li, X.-S.; et al. Difference analysis of shale reservoirs of Wufeng Formation and Longmaxi Formation in Changning area, southern Sichuan. *Fault-Block Oil Gas Field* **2021**, *28* (3), 289–294.

(44) Liu, Q.; Liang, B.; Sun, W.; Zhao, H.; Ghorbel, E. Experimental Study on the Difference of Shale Mechanical Properties. *Adv. Civ. Eng.* **2021**, *2021*, 1–14.

(45) Cui, Z.; Qi, S.; Han, W. The role of weak bedding planes in the cross-layer crack growth paths of layered rocks. *Geomech. Geophys. Geo-Energy Geo-Resour.* **2022**, *8* (1), 1–21.

(46) Han, W.; Peng, H.; Cui, Z.; et al. Influence of bedding plane strength on evolution of hydraulic fracture network. *J. Eng. Geol.* **2023**, *31* (6), 2030–2040.